I&EC research
Industrial & Engineering Chemistry Research
pubs.acs.org/IECR
Article

An Efficient Algorithm for Molecular Density Functional Theory in Cylindrical Geometry: Application to Interfacial Statistical Associating Fluid Theory (iSAFT)

Shun Xi, Jinlu Liu, Arjun Valiya Parambathu, Yuchong Zhang, and Walter G. Chapman*

Cite This: *Ind. Eng. Chem. Res.* 2020, 59, 6716−6728
Read Online

ABSTRACT: In this work, we present an efficient numerical algorithm for the solution of molecular density functional theory (DFT) in cylindrical geometry to facilitate the study of how curvature affects the microstructure and phase behavior of inhomogeneous fluids. The new solution algorithm is shown to have a better time scaling than the elliptic function method by Malijevskỳ [*J. Chem. Phys.* **2007**, *126*, 134710] and the transform method by Lado [*J. Comput. Phys.* **1971**, *8*, 417−433]. Convergence, performance, and stability of the numerical algorithm are discussed. We showcase two representative applications of the new method for modeling fluid adsorption and bottlebrush polymers using a specific DFT, interfacial statistical associating fluid theory (iSAFT). By comparing iSAFT with molecular simulation results, we found that iSAFT predicts layering transitions above the triple point for methane adsorption, and it captures power-law to parabolic transitions for polymer brush microstructure.

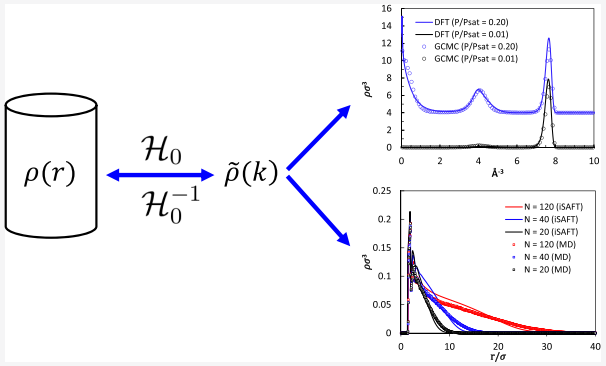

1. INTRODUCTION

In recent years, classical density functional theory (DFT) has been successfully applied to study the microscopic structure of inhomogeneous fluids after the successful introduction of fundamental measure theory (FMT) by Rosenfeld[1] and to model complex polymeric fluids with the extension of chain connectivity based on Wertheim's theory.[2,3] When a fluid experiences an external field, inhomogeneous phenomena such as fluid adsorption, capillary condensation, self-assembly, etc., are observed. While density functional theory accurately predicts the equilibrium fluid structure with a three-dimensional degree of freedom, it is prevalent to set the fluid distribution as one-dimensional (1D) in space by assuming density symmetry parallel to an interface, for example, fluid adsorbed in a slit-pore, cylindrical pore, and spherical cavity and polymer tethered to a planar wall, cylindrical nanorod, and spherical nanoparticle. Mathematical manipulations are necessary to reduce density functional theory from a three-dimensional formulation to a one-dimensional formulation. The planar geometry DFT formulation can be easily obtained since the vectorial notations in weighted densities remain unchanged in Cartesian coordinates. The polar geometry formulations such as cylindrical and spherical situations are more involved.[4] DFT in spherical geometry can be formulated using elementary functions.[5] However, cylindrical DFT formulation requires successive calculations of elliptic functions of the first and second kinds as provided by Malijevskỳ.[6] The implementation of the cylindrical DFT formulation by direct integration is thus nontrivial.

The Fourier transform method becomes an alternative route to solve density functional theory. The convolutional weighted densities and functional derivatives in DFT can be efficiently calculated in Fourier space. An early attempt in applying the Fourier transform to solve density functional theory was studied by Sears and Frink.[7] However, different numerical challenges arise in cylindrical geometry. The Fourier transform of DFT in cylindrical geometry has to be completed by the zeroth-order Hankel transform.

The Hankel transform naturally appears in many physical problems when the Fourier transform is applied to a cylindrically symmetric system. In optical theory, the Hankel transform provides a method to solve the paraxial wave equation, which describes the dynamics of cylindrical electromagnetic waves such as a laser beam.[8] In quantum mechanics, the Hankel transform is the key part in the pseudospectral method,[9] which effectively calculates the radial part of the Laplacian operator of the Schrödinger equation, and it provides a reduction in grid size compared with the finite

Received: December 18, 2019
Revised: February 27, 2020
Accepted: March 6, 2020
Published: March 6, 2020

https://dx.doi.org/10.1021/acs.iecr.9b06895
Ind. Eng. Chem. Res. 2020, 59, 6716−6728

difference method.[10] In statistical mechanics of equilibrium fluids, the Hankel transform can be applied to solve convolution-type integral equations by algebraically solving the transformed integral equation in Fourier space.[11] A classical example is the Ornstein−Zernike equation that defines the direct correlation function. Lado[11] provides a finite domain numerical implementation of Hankel transform by imposing a vanishing condition at the boundary. This method requires a matrix kernel to complete the transform. Therefore, it is not an efficient implementation compared to the standard fast Fourier transform (FFT) method. Siegman provides a quasi-fast Hankel transform (QFHT) by applying an exponential transformation.[12,13] Magni et al. modified Siegman's formulation and provided a fast Hankel transform with high accuracy.[14] This formulation only requires vector kernel to complete the transform in which an efficient FFT algorithm can be applied. In this work, we extend the use of fast Hankel transform as an efficient algorithm for the solution of interfacial statistical associating fluid theory (iSAFT).

Interfacial statistical associating fluid theory (iSAFT), a particular classical density functional theory by Tripathi and Chapman[15] and Jain et al.,[16] is an extension of statistical associating fluid theory (SAFT)[17] for inhomogeneous fluid. It has the advantage of modeling complex molecules beyond spherical shapes by including short-ranged association for water and alcohol,[18] homogeneous chain connectivity for hydrocarbons,[19] heterogeneous chain connectivity for block copolymers,[20] and branching effect for dendrimers[21] and star polymers.[22]

The previous studies using iSAFT focus on systems in planar geometry. However, including curvature is important to understand the equilibrium properties of inhomogeneous fluids at nanoscale and mesoscale. The vapor pressure of forming a spherical nanodroplet depends on both surface tension and the droplet radii.[23] Roth et al.[24] using density functional theory showed that the depletion forces near curved surfaces strongly deviate from the flat wall limit. The curvature effect has to be considered for modeling forces exerted onto the colloidal particles enclosed in vesicles. For hard-sphere fluids having curved interfaces, the surface tensions are shown proportional to the logarithm of the radius of interface curvature by using density functional theory.[25] Forsman and Woodward[26] studied the colloidal force between two spherical colloids dissolved in polymers using DFT of ideal chains with generalized Flory dimer (GFD) free energy functional. Excellent agreement was found with the Derjaguin approximation.[27] Hlushak used density functional theory of hard-sphere and Yukawa potential to study the optimal pore size for gas storage in fluid adsorption. It is found that the optimal pore size of a cylindrical pore is significantly more dependent on bulk pressure than slit-pore.[28] For long-chain polymers, Binder et al.[29] reported that cylindrical polymer brushes have two distinctive structures at low and high cylinder radius compared to flat polymer brushes. Therefore, it is necessary to continuously extend the applications of iSAFT to curved systems. Interesting systems of inhomogeneous fluids under spherical geometry have been investigated using iSAFT. These include the excellent agreement versus molecular simulation for the potential of mean force between colloids in a polymer melt[30] and self-assembled micelle formation.[5,31] In this work, we developed an efficient algorithm for iSAFT in cylindrical geometry as a tool for more specialized problems. We detail two applications of iSAFT in cylindrical geometry. The first case is the adsorption of methane in a cylindrical pore with Steele potential. The second case is bottlebrush polymers in implicit solvents. Given the versatility of iSAFT for accurately modeling spherical molecules and chain molecules, the development of an efficient solution algorithm for iSAFT will lead to further studies of complex fluids under cylindrical geometry.

The article is outlined as follows: Section 2 describes the theoretical framework of iSAFT free energy functional. Section 3 details the implementation of the algorithm. Section 4 verifies the algorithm and discusses the performance, convergence, and stability of the new algorithm. Section 5 showcases how it can be applied to modeling fluid adsorption in cylindrical nanopores and to modeling bottlebrush polymers.

2. ISAFT FREE ENERGY FUNCTIONAL

Density functional theory states that the equilibrium density distribution of inhomogeneous fluids is determined by the minimization of grand potential

$$\Omega[\rho] = A[\rho] - \sum_{\alpha} \int \mathrm{d}\mathbf{r}\, \rho_{\alpha}(\mathbf{r})[\mu_{\alpha} - V_{\alpha}^{\mathrm{ext}}(\mathbf{r})]$$

The minimization of grand potential produces the Euler−Lagrange equation

$$\frac{\delta\Omega[\rho]}{\delta\rho_{\alpha}(\mathbf{r})} = \frac{\delta A[\rho]}{\delta\rho_{\alpha}(\mathbf{r})} - (\mu_{\alpha} - V_{\alpha}^{\mathrm{ext}}(\mathbf{r})) = 0 \tag{1}$$

This is solved iteratively to obtain the equilibrium density distribution. $\Omega[\rho]$ and $A[\rho]$ are the total grand potential and Helmholtz free energy functional of the system, respectively. $\rho_{\alpha}(\mathbf{r})$ is the spatial density distribution of component α. μ_{α} is the chemical potential of component α. $V_{\alpha}^{\mathrm{ext}}(\mathbf{r})$ is the external potential for component α.

The free energy functional of iSAFT is based on perturbation theory that the Helmholtz free energy can be decomposed into reference fluid and perturbation

$$A[\rho] = A^{\mathrm{id}}[\rho] + A^{\mathrm{hs}}[\rho] + A^{\mathrm{disp}}[\rho] + A^{\mathrm{ch}}[\rho]$$

where $A^{\mathrm{id}}[\rho]$, $A^{\mathrm{hs}}[\rho]$, $A^{\mathrm{disp}}[\rho]$, $A^{\mathrm{ass}}[\rho]$, and $A^{\mathrm{ch}}[\rho]$ are free energy functional of ideal gas contribution, hard-sphere contribution, dispersion contribution, association, and chain contribution. The Euler−Lagrange equation (eq 1) under the framework of perturbation theory is

$$\frac{\delta A^{\mathrm{id}}[\rho]}{\delta\rho_{\alpha}(\mathbf{r})} + \frac{\delta A^{\mathrm{hs}}[\rho]}{\delta\rho_{\alpha}(\mathbf{r})} + \frac{\delta A^{\mathrm{disp}}[\rho]}{\delta\rho_{\alpha}(\mathbf{r})} + \frac{A^{\mathrm{ass}}[\rho]}{\delta\rho_{\alpha}(\mathbf{r})} + \frac{A^{\mathrm{ch}}[\rho]}{\delta\rho_{\alpha}(\mathbf{r})} = (\mu_{\alpha} - V_{\alpha}^{\mathrm{ext}}(\mathbf{r})) \tag{2}$$

The ideal gas functional is

$$A^{\mathrm{id}}[\rho] = k_{\mathrm{B}}T \sum_{\alpha} \int \mathrm{d}\mathbf{r}\, \rho_{\alpha}(\mathbf{r})[\ln(\rho_{\alpha}(\mathbf{r})) - 1]$$

and the functional derivative for ideal gas contribution is

$$\frac{\delta A^{\mathrm{id}}[\rho]}{\delta\rho_{\alpha}(\mathbf{r})} = k_{\mathrm{B}}T \ln \rho_{\alpha}(\mathbf{r}) \tag{3}$$

We use fundamental measure theory to approximate the reference hard-sphere fluid free energy functional $A^{\mathrm{hs}}[\rho]$. Fundamental measure theory constructs the free energy density functional by weighting singlet fluid density using

https://dx.doi.org/10.1021/acs.iecr.9b06895
Ind. Eng. Chem. Res. 2020, 59, 6716−6728

geometric properties of spheres. These weighted densities $n_i[\rho(\mathbf{r})]$ are surface averaged, volume averaged, mean curvature averaged, and Gaussian curvature averaged densities. The free energy functional is[4]

$$A^{\mathrm{hs}}[\rho] = k_{\mathrm{B}}T \int \mathrm{d}\mathbf{r}\, \Phi[n_i(\mathbf{r})] \tag{4}$$

and the hard-sphere free energy density $\Phi[n_i(\mathbf{r})]$ is given by

$$\begin{aligned}\Phi(\mathbf{r}) = &-n_0(\mathbf{r}) \ln(1 - n_3(\mathbf{r})) \\ &+ \frac{n_1(\mathbf{r})n_2(\mathbf{r}) - \mathbf{n}_{v1}(\mathbf{r})\cdot\mathbf{n}_{v2}(\mathbf{r})}{1 - n_3(\mathbf{r})} \\ &+ \frac{n_2(\mathbf{r})^3 - 3n_2(\mathbf{r})\mathbf{n}_{v2}(\mathbf{r})\cdot\mathbf{n}_{v2}(\mathbf{r})}{24\pi(1-n_3(\mathbf{r}))^2}\end{aligned} \tag{5}$$

The functional derivative for the hard-sphere contribution reads

$$\frac{\delta A^{\mathrm{hs}}[\rho]/k_{\mathrm{B}}T}{\delta\rho_\alpha(\mathbf{r})} = \sum_{i=0,1,2,3,v1,v2} \frac{\partial\Phi}{\partial n_i(\mathbf{r}')} * \omega_\alpha^{(i)}(\mathbf{r} - \mathbf{r}') \tag{6}$$

where * denotes spatial convolution.

The calculations of the weighted densities and the functional derivative for the hard-sphere contribution require a few special treatments for cylindrical geometry. A detailed implementation is provided in the Supporting Information of this work.

The dispersion contribution is calculated by applying the weighed density approximation (WDA) approach to the perturbed-chain SAFT (PC-SAFT)[32] bulk free energy. The WDA approach is similar to the method introduced by Sauer and Gross.[33] This method has been shown to provide an accurate prediction for interfacial tension of mixtures and the inhomogeneous free energy density reduces to the free energy of PC-SAFT in the bulk limit. The key part of the WDA approach is the weighted density field

$$\begin{aligned}\overline{\rho}_\alpha(\mathbf{r}) &= \frac{1}{\frac{4}{3}\pi d_\alpha^3} \int \rho_\alpha(\mathbf{r}')\Theta(d_\alpha - |\mathbf{r}-\mathbf{r}'|)\, \mathrm{d}\mathbf{r}' \\ &= \rho_\alpha(\mathbf{r}) * \omega_\alpha^{\mathrm{avg}}(|\mathbf{r}-\mathbf{r}'|)\end{aligned} \tag{7}$$

where $\Theta(r)$ denotes the Heaviside step function and d_α is the segment diameter for component α. The body average weighting function is

$$\omega_\alpha^{\mathrm{avg}}(|\mathbf{r}-\mathbf{r}'|) = \frac{3}{4\pi d_\alpha^3}\Theta(d_\alpha - |\mathbf{r}-\mathbf{r}'|)$$

d_α is the temperature-dependent hard-sphere diameter of component α as used in PC-SAFT[32]

$$d_\alpha = \sigma_\alpha\left[1 - 0.12 \exp\left(-3\frac{\epsilon_\alpha}{k_{\mathrm{B}}T}\right)\right]$$

From the coarse-grained weighted density field, the inhomogeneous PC-SAFT dispersion Helmholtz free energy functional can be determined by the following

$$A^{\mathrm{disp}}[\rho] = k_{\mathrm{B}}T \int \overline{\rho}(\mathbf{r})\tilde{a}^{\mathrm{disp}}(\overline{\rho}_\alpha(\mathbf{r}))\, \mathrm{d}\mathbf{r} \tag{8}$$

where $\overline{\rho}_\alpha(\mathbf{r})$ is the weighted density distribution given in eq 7. Here, $\tilde{a}^{\mathrm{disp}}(\overline{\rho}_\alpha(\mathbf{r}))$ denotes the PC-SAFT dispersion free energy density calculated with the weighted density field

$$\begin{aligned}\tilde{a}^{\mathrm{disp}}(\overline{\rho}_\alpha(\mathbf{r})) = &-2\pi\overline{\rho}(\mathbf{r})I_1(\overline{\eta}, \overline{m})\overline{m^2\epsilon\sigma^3} \\ &- \pi\overline{\rho}(\mathbf{r})\overline{m}C_1I_2(\overline{\eta}, \overline{m})\overline{m^2\epsilon^2\sigma^3}\end{aligned} \tag{9}$$

The total weighted density for mixture is a sum of all of the individual partial densities

$$\overline{\rho}(\mathbf{r}) = \sum_\alpha \overline{\rho}_\alpha(\mathbf{r})$$

and the mean PC-SAFT segment number is

$$\overline{m} = \sum_\alpha \overline{x}_\alpha m_\alpha$$

The other terms in the free energy density $\tilde{a}^{\mathrm{disp}}(\overline{\rho}_\alpha(\mathbf{r}))$ are given by

$$\overline{x}_\alpha = \overline{\rho}_\alpha(\mathbf{r})/\overline{\rho}(\mathbf{r})$$

$$\overline{\eta}(\mathbf{r}) = \frac{\pi}{6}\sum_\alpha \overline{\rho}_\alpha(\mathbf{r})m_\alpha\sigma_\alpha^3$$

$$\overline{m^2\epsilon^n\sigma^3} = \sum_\alpha\sum_\beta \overline{x}_\alpha\overline{x}_\beta m_\alpha m_\beta\left(\frac{\epsilon_{\alpha\beta}}{k_{\mathrm{B}}T}\right)^n\sigma_{\alpha\beta}^3$$

$$C_1 = \left[1 + \overline{m}\frac{8\overline{\eta} - 2\overline{\eta}^2}{(1-\overline{\eta})^4} + (1-\overline{m})\frac{20\overline{\eta} - 27\overline{\eta}^2 + 12\overline{\eta}^3 - 2\overline{\eta}^4}{(1-\overline{\eta})^2(2-\overline{\eta})^2}\right]^{-1}$$

The universal integral I_1 and I_2 and the molecular parameters σ_α, ϵ_α, and m_α are the same as the ones used by PC-SAFT equation of state.[32]

The calculation of the functional derivative due to dispersion contribution is obtained by differentiating the Helmholtz free energy given in eq 8

$$\frac{\delta A^{\mathrm{disp}}[\rho]/k_{\mathrm{B}}T}{\delta\rho_\alpha(\mathbf{r})} = \frac{\partial[\overline{\rho}(\mathbf{r})\tilde{a}^{\mathrm{disp}}(\overline{\rho}_\alpha(\mathbf{r}))]}{\partial\overline{\rho}_\alpha(\mathbf{r})} * \omega_\alpha^{\mathrm{avg}}(|\mathbf{r}-\mathbf{r}'|) \tag{10}$$

The associating free energy functional was first developed by Segura and Chapman[34,35] for inhomogeneous fluids. It is further extended to associating polymer by Bymaster and Chapman[22]

$$A^{\mathrm{ass}}[\rho] = k_{\mathrm{B}}T \int \mathrm{d}\mathbf{r}' \sum_\alpha \rho_\alpha(\mathbf{r}') \sum_{\mathrm{A}_\alpha}\left(\ln\chi_{\mathrm{A}_\alpha}(\mathbf{r}') - \frac{\chi_{\mathrm{A}_\alpha}(\mathbf{r}')}{2} + \frac{1}{2}\right) \tag{11}$$

where $\chi_{\mathrm{A}_\alpha}(\mathbf{r})$ is the fraction of segment α at position $\mathbf{r}$ not bonded at site A. The inhomogeneous unbonded fraction involves solving integral equations in real space to provide an accurate degree of association

$$\chi_{\mathrm{A}_\alpha}(\mathbf{r}) = \left[1 + \int \mathrm{d}\mathbf{r}' \sum_\beta \rho_\beta(\mathbf{r}') \sum_{\mathrm{B}_\beta} \chi_{\mathrm{B}_\beta}(\mathbf{r}')\Delta^{\mathrm{A}_\alpha\mathrm{B}_\beta}(\mathbf{r}, \mathbf{r}')\right]^{-1} \tag{12}$$

The association strength is similar to its original form in SAFT except that it contains an inhomogeneous cavity function

https://dx.doi.org/10.1021/acs.iecr.9b06895
Ind. Eng. Chem. Res. 2020, 59, 6716−6728

$$\Delta^{A_\alpha B_\beta}(\mathbf{r}, \mathbf{r}') = \kappa[\exp(\beta\epsilon^{ass}_{A_\alpha B_\beta}) - 1]y^{\alpha\beta}(\mathbf{r}, \mathbf{r}') \quad (13)$$

where κ is a constant that includes the bonding volume and orientation constraints and $\epsilon^{ass}_{A_\alpha B_\beta}$ is the association energy between site A and site B from species α and β, respectively. We approximate the inhomogeneous correlation function $y^{\alpha\beta}(\mathbf{r}, \mathbf{r}')$ for the reference hard-sphere fluid between segment α and β as the geometric average of bulk radial distribution functions at contact evaluated at average density $\overline{\rho}_\alpha(\mathbf{r})$[15]

$$y^{\alpha\beta}(\mathbf{r}, \mathbf{r}') = [g_{\alpha\beta}(\overline{\rho}(\mathbf{r}), \sigma_{\alpha\beta})]^{1/2}[g_{\alpha\beta}(\overline{\rho}(\mathbf{r}'), \sigma_{\alpha\beta})]^{1/2} \quad (14)$$

The functional derivative of association contribution is

$$\frac{\delta A^{ass}/k_BT}{\delta\rho_\alpha(\mathbf{r})} = \sum_{A_\alpha} \ln \chi_{A_\alpha}(\mathbf{r}) - \frac{1}{2}\int d\mathbf{r}' \sum_\gamma \sum_\beta \rho_\beta(\mathbf{r}') \sum_{B_\beta} (1 - \chi_{B_\beta}(\mathbf{r}'))\left[\frac{\delta \ln y^{\gamma\beta}(\mathbf{r}')}{\delta\rho_\alpha(\mathbf{r})}\right] \quad (15)$$

The chain free energy functional derivative is derived from the association free energy functional at the limit of complete association[16]

$$\frac{\delta A^{ch}/k_BT}{\delta\rho_\alpha(\mathbf{r})} = \sum_{A_\alpha} \ln \chi_{A_\alpha}(\mathbf{r}) - \frac{1}{2}\int d\mathbf{r}' \sum_\beta \sum_{\beta'} \rho_\beta(\mathbf{r}') \left[\frac{\delta \ln y^{\beta\beta'}(\mathbf{r}')}{\delta\rho_\alpha(\mathbf{r})}\right] \quad (16)$$

here β' refers to all of the segments that are bonded to segment β.

By substituting functional derivatives (eqs 3, 6, 10, 15, and 16) into Euler−Lagrange equation (eq 1), equilibrium density distributions can be solved by

$$\rho_\alpha(\mathbf{r}) = \exp(\beta\mu_M) \exp[D_\alpha(\mathbf{r}) - \beta V_\alpha^{ext}(\mathbf{r})] I_{1,\alpha}(\mathbf{r}) I_{2,\alpha}(\mathbf{r}) \quad (17)$$

where

$$D_\alpha(\mathbf{r}) = -\frac{\delta A^{hs}/k_BT}{\delta\rho_\alpha(\mathbf{r})} - \frac{\delta A^{disp}/k_BT}{\delta\rho_\alpha(\mathbf{r})} - \frac{\delta A^{ass}/k_BT}{\delta\rho_\alpha(\mathbf{r})} + \frac{1}{2}\int d\mathbf{r}' \sum_\beta \sum_{\beta'} \rho_\beta(\mathbf{r}')\left[\frac{\delta \ln y^{\beta\beta'}(\mathbf{r}')}{\delta\rho_\alpha(\mathbf{r})}\right] \quad (18)$$

and μ_M is the bulk molecular chemical potential given by a summation of bulk segment chemical potential μ_α of a chain

$$\mu_M = \sum_\alpha^m \mu_\alpha \quad (19)$$

Here, m is the total number of segments. Two recursive integrals $I_{1,\alpha}$ and $I_{2,\alpha}$ are essential to model chain molecules. Information of covalent bonding is recursively shared among all of the segments of polymers by a recurrence equation. Their explicit forms are

$$I_{1,\alpha}(\mathbf{r}) = \int d\mathbf{r}' \, I_{1,\alpha-1}(\mathbf{r}') \exp[D_{\alpha-1}(\mathbf{r}')]\Delta^{\alpha-1,\alpha}(\mathbf{r}', \mathbf{r}) \quad (20)$$

and

$$I_{2,\alpha}(\mathbf{r}) = \int d\mathbf{r}' \, I_{2,\alpha+1}(\mathbf{r}') \exp[D_{\alpha+1}(\mathbf{r}')]\Delta^{\alpha,\alpha+1}(\mathbf{r}', \mathbf{r}) \quad (21)$$

The boundary conditions for I_1 and I_2 are $I_{1,1} = 1$ and $I_{2,m} = 1$.

3. FAST HANKEL TRANSFORM ALGORITHM

3.1. Fourier Transform in Cylindrical Geometry. Solving the Euler−Lagrange equation (eq 1) requires iterative calculation of weighted densities and functional derivatives (eqs 6, 10, 15, and 16), which are computationally expensive since convolutions are involved. A natural approach to circumvent this step is to apply the convolution theorem and the FFT algorithm. Comparing with directly solving the Euler−Lagrange equation (eq 1), utilizing the FFT algorithm usually provides a speedup from $O(N^2)$ to $O(N \log N)$. This method is well applied to a system with Cartesian mesh.[7]

The forward and backward two-dimensional Fourier transform of a two-dimensional function are

$$g(\mathbf{k}) = \int f(\mathbf{r}) \exp(i\mathbf{k}\cdot\mathbf{r}) \, d\mathbf{r} \quad (22)$$

$$f(\mathbf{r}) = \frac{1}{(2\pi)^2}\int g(\mathbf{k}) \exp(-i\mathbf{k}\cdot\mathbf{r}) \, d\mathbf{k} \quad (23)$$

where $f(\mathbf{r}) = f(x, y)$ and $g(\mathbf{k}) = g(k_x, k_y)$. If the function $f(\mathbf{r})$ is a circularly symmetric function, i.e., $f(\mathbf{r}) = f(r)$ with $r = \sqrt{x^2 + y^2}$, its Fourier transform is also a circularly symmetric function $g(\mathbf{k}) = g(k)$ with $k = \sqrt{k_x^2 + k_y^2}$. More precisely, the forward and backward Fourier transforms of a circular symmetric function are Hankel transforms of zeroth-order

$$g(k) = 2\pi\int_0^\infty rf(r)J_0(2\pi rk) \, dr \quad (24)$$

$$f(r) = 2\pi\int_0^\infty kg(k)J_0(2\pi rk) \, dk \quad (25)$$

For inhomogeneous fluid in cylindrical geometry, the density distribution $\rho_\alpha(\mathbf{r})$ reduces to $\rho_\alpha(r)$. Equations 22 and 23 reduce to Hankel transform

$$\tilde{\rho}_\alpha(k) = 2\pi\int_0^\infty r\rho_\alpha(r)J_0(2\pi kr) \, dr \quad (26)$$

$$\rho_\alpha(r) = 2\pi\int_0^\infty k\tilde{\rho}_\alpha(k)J_0(2\pi kr)dk \quad (27)$$

where $\tilde{\rho}_\alpha(k)$ is the Hankel transform of density distribution $\rho_\alpha(r)$ in cylindrical geometry. J_0 is zeroth-order Bessel function of the first kind. Now, eqs 26 and 27 are Hankel transforms of zeroth-order. Equations 26 and 27 have to be numerically calculated. Lado[11] introduced the finite discretized Hankel transform by using the orthogonality between the zeroth-order and first-order Bessel functions. By substituting $q = 2\pi k$ for $2\pi k$ in eqs 26 and 27, the discrete transform can be obtained by considering the procedure by Lado[11]

$$\tilde{\rho}_\alpha(q_j) = \sum_{i=1}^N \frac{4\pi J_0(q_j r_i)}{q_N^2 J_1^2(z_i)}\rho_\alpha(r_i) \quad (28)$$

and its backward transform is

$$\rho_\alpha(r_i) = \sum_{j=1}^N \frac{J_0(q_j r_i)}{\pi r_N^2 J_1^2(z_j)}\tilde{\rho}_\alpha(q_j) \quad (29)$$

https://dx.doi.org/10.1021/acs.iecr.9b06895
Ind. Eng. Chem. Res. 2020, 59, 6716−6728

The r_i and q_j are discretized real space grid and Fourier space grid, respectively, and z_i is the ith zero of J_0. Equations 28 and 29 are matrix−vector products and the computation scales as $O(N^2)$ with N as the number of mesh grid. Lado's method[11] therefore does not provide an efficient $O(N \log N)$ time scaling.

3.2. Fast Hankel Transform. Additional speedup in computing functional derivatives can be achieved by exploiting a transformation of variables.[14] The space variable r and frequency variable k are first normalized by a spatial domain cut-off b and a frequency cut-off λ. The function $f(r)$ vanishes when r is beyond b, more precisely $f(r) = 0$ if $r \geq b$. The space cut-off and the frequency cut-off are related by the space-bandwidth product $\gamma = \lambda b$.

By substituting with normalized variables, $x = r/b$ and $y = k/\lambda$, the truncated and normalized Hankel transforms (eqs 24 and 25) are

$$g(y) = 2\pi\gamma \frac{b}{\lambda} \int_0^1 x f(x) J_0(2\pi\gamma x y)\, \mathrm{d}x \tag{30}$$

$$f(x) = 2\pi\gamma \frac{\lambda}{b} \int_0^1 y g(y) J_0(2\pi\gamma x y)\, \mathrm{d}y \tag{31}$$

To numerically compute eqs 30 and 31, the domain, i.e., $0 \leq x \leq 1$ needs to be further divided into N subintervals by selecting the partition points χ_i, where $0 = \chi_0 < \chi_1 < \cdots < \chi_N = 1$. The original function $f(x)$ is evaluated at x_i ($i = 0, 1, ..., N-1$), where $\chi_i \leq x_i \leq \chi_{i+1}$. $f(x_N) = 0$ is set as a boundary condition. The subintervals are defined in this way such that there is exactly one point x_i per subinterval. Because of the partition, it is reasonable to assume that $f(x) \approx f(x_i)$ for x within the interval, i.e., $\chi_i < x_i < \chi_{i+1}$. The divided integral of eqs 30 and 31 for each subinterval can be expressed as

$$\int_{\chi_i}^{\chi_{i+1}} x f(x) J_0(2\pi\gamma y x)\, \mathrm{d}x = \frac{f(x_i)}{2\pi\gamma y}[J_1(2\pi\gamma y \chi_{i+1})\chi_{i+1} - J_1(2\pi\gamma y \chi_i)\chi_i] \tag{32}$$

where the second part of eq 32 is an analytical result if we apply the approximation $f(x) \approx f(x_i)$ for $\chi_i < x_i < \chi_{i+1}$ and realize the fact $\int x J_0(x)\, \mathrm{d}x = x J_1(x) + C$. Summing over all of the intervals and considering two boundary conditions $J_1(0) = 0$ and $f(x_N) = 0$, eq 30 can be numerically evaluated

$$g(y) = \frac{b}{\lambda y} \sum_{i=0}^{N-1} [f(x_i) - f(x_{i+1})] J_1(2\pi\gamma y \chi_{i+1})\chi_{i+1} \tag{33}$$

The discretization process is based on exponential transformation. A natural approach to set the partition point χ_i is

$$\chi_i = 0 \quad \text{for } i = 0$$
$$\chi_i = \mathrm{e}^{\alpha(i-N)} \quad \text{for } i = 1, 2, ..., N \tag{34}$$

such that $0 = \chi_0 < \chi_1 < \cdots < \chi_N = 1$ is satisfied.

The grids for x_i and y_j are also nonequidistant

$$x_i = x_0\, \mathrm{e}^{\alpha i} \quad \text{for} \quad i = 0, 1, 2, ..., N-1 \tag{35}$$

$$y_j = x_0\, \mathrm{e}^{\alpha j} \quad \text{for} \quad j = 0, 1, 2, ..., N-1 \tag{36}$$

The reason for applying the exponential transformation is evident by analyzing the general Hankel transforms (eqs 24 and 25). If we treat the continuous variables r and k in eqs 24 and 25 as $r = r_0\, \mathrm{e}^{\alpha u}$ and $k = r_0\, \mathrm{e}^{\alpha v}$ and substitute them into eqs 24 and 25, we end up with the following cross-correlations that can be efficiently evaluated by the FFT algorithm

$$\hat{g}(v) = 2\pi \int_{-\infty}^{\infty} \hat{f}(u)\hat{j}(u+v)\, \mathrm{d}u \tag{37}$$

$$\hat{f}(u) = 2\pi \int_{-\infty}^{\infty} \hat{g}(v)\hat{j}(u+v)\, \mathrm{d}v \tag{38}$$

where $\hat{f}(u) = rf(r)$, $\hat{g}(v) = kg(k)$, and $\hat{j}(u+v) = \alpha r k J_0(2\pi r k)$.

If we apply the discretization (eqs 35 and 36 to eq 33), we obtain $\tilde{g}(y_j)$, a discretized $g(y)$

$$\tilde{g}(y_j) = \frac{b}{\lambda y_j} \sum_{i=0}^{N-1} k_i [f(x_i) - f(x_{i+1})]\, \mathrm{e}^{\alpha(i+1-N)} J_1(2\pi\gamma x_0\, \mathrm{e}^{\alpha(i+j+1-N)}) \tag{39}$$

Now, eq 39 can also be treated as a discrete cross-correlation

$$\tilde{g}(y_j) = \frac{b}{\lambda y_j} \sum_{i=0}^{N-1} \tilde{\phi}_i \tilde{j}_{i+j} \tag{40}$$

where we define

$$\tilde{\phi}_i = \begin{cases} k_i [f(x_i) - f(x_{i+1})]\, \mathrm{e}^{\alpha(i+1-N)} & \text{for} \quad i = 0, ..., N-1 \\ 0 & \text{for} \quad i = N, ..., 2N-1 \end{cases}$$

and the kernel

$$\tilde{j}_{i+j} = J_1(2\pi\gamma x_0\, \mathrm{e}^{\alpha(i+j-1-N)})$$

We can apply the efficient FFT algorithm to calculate eq 40

$$\tilde{g}(y_j) = \frac{b}{\lambda y_j} \mathcal{F}\{\mathcal{F}\{\tilde{\phi}_i\}\mathcal{F}^{-1}\{\tilde{j}_{i+j}\}\}$$

where $\mathcal{F}$ is forward Fourier transform and $\mathcal{F}^{-1}$ is inverse Fourier transform.

It is worthwhile to note that α and x_0 in eq 39 are free parameters to be determined. To ensure that every x_i lies in between χ_i and χ_{i+1} for $i = 1, 2, ..., N-1$, an inequality needs to be satisfied

$$\mathrm{e}^{\alpha(i-N)} < x_0\, \mathrm{e}^{\alpha i} < \mathrm{e}^{\alpha(i+1-N)}$$
$$\mathrm{e}^{-\alpha N} < x_0 < \mathrm{e}^{\alpha(1-N)} \tag{41}$$

Equation 41 suggests the average of its upper bound and lower bounds is a good choice for x_0, i.e., $x_0 = [\mathrm{e}^{-\alpha N} + \mathrm{e}^{\alpha(1-N)}]/2$. Because x_0 does not lie in between χ_i and χ_{i+1}, $f(x) \approx f(x_0)$ is an erroneous approximation for $\chi_0 < x < \chi_1$. Hence, the factor k_0 is an end correction factor[36] to correct the approximation for the end subinterval including the origin. The correction factor k_i is

$$k_i = \begin{cases} 1 & \text{for} \quad i \neq 0 \\ \dfrac{\mathrm{e}^{2\alpha}(2\mathrm{e}^{\alpha} + \mathrm{e}^{2\alpha} - 1)}{(1 + \mathrm{e}^{\alpha})^2(\mathrm{e}^{2\alpha} - 1)} & \text{for} \quad i = 0 \end{cases} \tag{42}$$

The derivation of the end correction factor arises from substituting $f(x_0)$ with $f(x_0^{\dagger})$, where $f(x_0^{\dagger})$ is the function $f(x)$ evaluated at a fictitious end $x_0^{\dagger}$. We interpolate $f(x)$ for $x \leq x_1$ by quadratic parabola $f(x) = a_2x^2 + a_0$, which has no first-order

https://dx.doi.org/10.1021/acs.iecr.9b06895
Ind. Eng. Chem. Res. 2020, 59, 6716−6728

term since we assume that the first-order derivative of the quadratic parabola vanishes at the origin. $f(x_0^\dagger)$ is an analytical result of eq 32, i.e., $\int_{\chi_0}^{\chi_1} xf(x)J_0(2\pi\gamma yx)\,dx = \frac{f(x_0^\dagger)}{2\pi\gamma y}J_1(2\pi\gamma y\chi_1)$. More precisely

$$\begin{aligned} f(x_0^\dagger) &= 2\pi\gamma y\frac{\int_{\chi_0}^{\chi_1} xf(x)J_0(2\pi\gamma yx)\,dx}{J_1(2\pi\gamma y\chi_1)} \\ &= 2\pi\gamma y\frac{\int_{\chi_0}^{\chi_1}(a_2x^3 + a_0x)J_0(2\pi\gamma yx)\,dx}{J_1(2\pi\gamma y\chi_1)} \\ &= a_2\chi_1\frac{2J_2(2\pi\gamma y\chi_1) - 2\pi\gamma y\chi_1 J_3(2\pi\gamma y\chi_1)}{2\pi\gamma y J_1(2\pi\gamma y\chi_1)} + a_0 \end{aligned} \tag{43}$$

We further simplify eq 43 by evaluating it at $y = 0$ so as to avoid the dependency on y and to eliminate low-frequency shift in practice. We obtain the correction factor k_0 in eq 42

$$\begin{aligned} f(x_0^\dagger) - f(x_1) &= \left(\frac{1}{2}a_2\chi_1^2 + a_0\right) - f(x_1) \\ &= \frac{1}{2}a_2\chi_1^2 + f(x_1) - a_2x_1^2 - f(x_1) \\ &= \frac{f(x_0) - f(x_1)}{x_0^2 - x_1^2}\left(\frac{1}{2}\chi_1^2 - x_1^2\right) \\ &= k_0[f(x_0) - f(x_1)] \end{aligned}$$

It comes to the authors' attention that Boţan et al.[37] previously introduced a fast Hankel transform for density functional theory. Boţan's treatment is similar to the original QFHT by Siegman[12] without the end correction term. The difference from this work is that we approximate the function as constant over each subinterval, which leads to the different kernel basis that we used. The time scaling of the implementation is similar to that in this work. Boţan's treatment also ignores the end correction term, i.e., it does not include the interval $0 < x < x_0$. The missing end correction term can possibly lead to divergence at the origin, which we will show in the next section. A more comprehensive discussion on end correction term can be seen in the reference.[36]

3.3. Choice of Parameters for Fast Hankel Transform. To apply the new algorithm, a few parameters have to be determined, such as the position of the first mesh, x_0, the maximum frequency cut-off, λ, the maximum space cut-off, b, the number of mesh points, N, and free transformation parameters, α. The accuracy of the algorithm depends on the bandwidth, γ, which is the product of λ and b. The choice of space cut-off b can be determined from a priori knowledge about the system domain such as cylindrical pore radius R.

The choice of frequency cut-off λ depends on the nature of function $f(x)$ itself, which is the density distribution $\rho(r)$ in this study. In our study, it is found that λ increases with the system domain size. An effective λ from 30 to 50 is used in this study when the dimensionless system domain size varies from $R^* = 3$ to 5. The number of grid points N is chosen to be from 2^9 to 2^{11} for varying system domains. A choice for x_0 has been given previously. Another free parameter α can be determined by setting the same width for the first and the last subintervals, i.e., $\chi_N - \chi_{N-1} = \chi_1 - \chi_0$.[1414] This gives a good choice for α: $\alpha = -\ln[1 - e^{\alpha(1-N)}]$.

Though it is desirable to have a higher frequency cut-off λ to capture the rapid oscillation of fluid distribution, it leads to insufficient sampling at high frequency. More grid points N always increases sampling effectiveness, but it is computationally expensive. A good criterion to balance these two parameters is to enforce the least number of cycles between two zeros of the Bessel kernel J_0. The difference between two zeros of Bessel function is approximately equal to π.[38] If there is at least one sampling between two zeros, then a relation based on eqs 30 and 31 is

$$2\pi\gamma x_0[e^{\alpha(N-1)} - e^{\alpha(N-2)}] < \pi \tag{44}$$

This inequality enforces that at least one Bessel zero is sampled over the last two sampling points where it has the largest grid spacing.

4. ANALYSIS OF THE ALGORITHM

In this section, we first compare the density distributions for hard-sphere fluids in cylindrical geometry by DFT solved by the proposed algorithm with the grand canonical Monte Carlo (GCMC) simulation by Malijevskỳ,[6] followed by a comprehensive analysis of convergence, performance, and stability of the algorithm.

4.1. Verification of the Algorithm by Binary Hard-Spheres in Hard Cylindrical Pores. Figure 1 shows the density distribution of a binary mixture of hard-spheres confined in hard cylindrical pores. The external potential of a hard cylindrical pore is given by

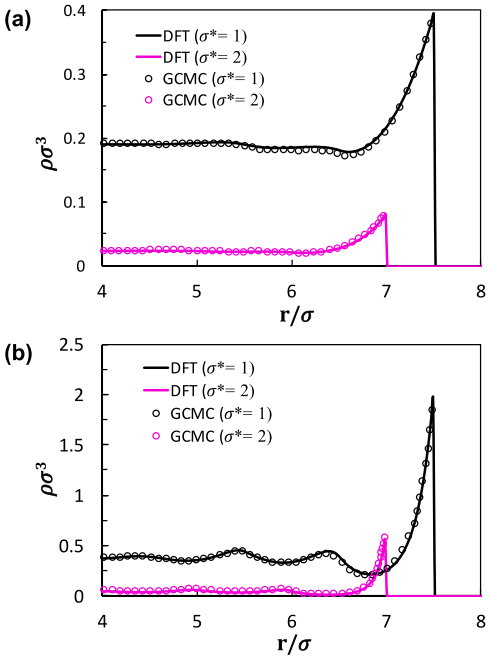

Figure 1. Binary mixture of hard-spheres of size ratio 2:1 in a hard cylindrical nanopore at overall bulk packing fraction (a) $\eta = 0.3$ and (b) $\eta = 0.4$. Solid lines are results from this work. Symbols are digitized molecular simulation results of Malijevskỳ.[6]

https://dx.doi.org/10.1021/acs.iecr.9b06895
Ind. Eng. Chem. Res. 2020, 59, 6716−6728

$$V_\alpha^{\text{ext}}(r) = \begin{cases} \infty & \text{for} \quad r > R - \dfrac{\sigma_\alpha}{2} \\ 0 & \text{for} \quad r \le R - \dfrac{\sigma_\alpha}{2} \end{cases}$$

Hard cylindrical pores with pore radii $R/\sigma_1 = 8$ and overall bulk packing fractions $\eta = 0.3$ and 0.4 are chosen. The packing fraction is defined by $\eta = \sum_\alpha \pi\rho_\alpha\sigma_\alpha^3/6$. The size ratio of large to small hard-spheres is set as $\sigma_2/\sigma_1 = 2$. Good agreement between molecular simulation and density functional theory solved by the new method is found from low to high packing densities, as shown in Figure 1a,b. At a low packing fraction $\eta = 0.3$, both theory and simulation show that there is little fluid structure except at the wall for both small and large particles. At a high packing fraction $\eta = 0.4$, the small particle has a three-layered strongly oscillatory fluid structure and two layers of large particles are adsorbed on the hard cylindrical wall.

4.2. Convergence, Performance, and Stability. Since we are interested in applying the new algorithm to density functional theory, here, we discuss the convergence, performance, and stability of the new algorithm. For simplicity and consideration of time, the analysis here is carried out for hard-sphere fluids in hard cylindrical pores of pore radii R^*_{max} and a bulk density $\rho^*_{\text{B}} = 0.8$. $\rho^* = \rho\sigma^3$ and $R^* = R/\sigma$ are dimensionless. The mixing fraction for Picard iteration is constant 1×10^{-2}. The grid size is set to $\Delta r^* = 0.02$ for Lado's method and Malijevskỳ's elliptic function method. Since the new algorithm has a nonequidistant grid, we set the last grid spacing for the new method to $\Delta r^*_{\text{max}} = 0.02$ for comparison.

The convergence is represented by using the residual norm

$$\epsilon = \left(\int (\rho^*_{k+1}(r^*) - \rho^*_k(r^*))^2 \, \mathrm{d}r^* \right)^{1/2}$$

where $\rho^* = \rho\sigma^3$ and $r^* = r/\sigma$. It is the square root of the total squared residual of all of the grids from the kth to the $(k+1)$th iteration in solving eq 1. The convergences of Malijevskỳ's elliptic function method, Lado's transform method, and this work are shown in Figure 2. It is interesting that the convergences of the elliptic function method and this work are similar. They both reach a residual norm 1×10^{-4} after 500 iterations. However, Lado's method has a slower convergence rate. It requires 4000 iterations to reduce the residual norm to 1×10^{-4}.

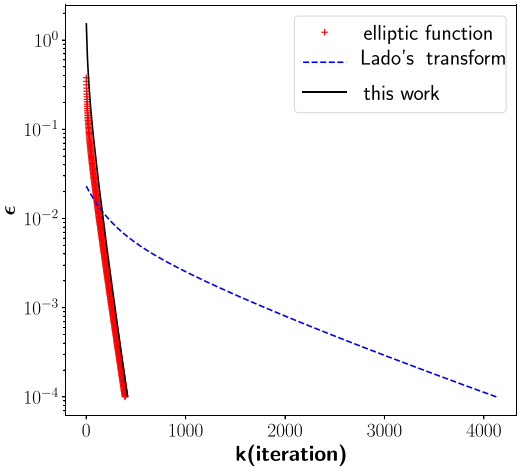

Figure 2. Residual norm changes with the number of Picard iterations for hard-spheres adsorbed in a hard cylindrical pore of radius $R^*_{\text{max}} = 8$ at reduced bulk density $\rho^*_{\text{B}} = 0.8$.

Though the convergence rates vary for different implementations, we are ultimately interested in knowing the machine time to solve density functional theory across different algorithms. Here, we show the scaling of time with respect to the system domain size since the grid spacing is not uniform for the new algorithm. The domain size R^*_{max} ranges from 2 to 16. We compare all of the three methods by enforcing the largest grid spacing of our method to be the same as the grid spacings of other methods. Lado's method is faster than the elliptic function method, as shown in Figure 3, though it has a slower convergence rate per iteration, as seen in Figure 2. This is because the computation of digamma functions required by the elliptic function method is very expensive.[6] The new algorithm is faster than Lado's method by another order of magnitude. Though they are both Fourier transform methods, Lado's method requires an $O(N^2)$ operation as discussed previously in eqs 26 and 27 compared to FFT's $O(N \log N)$ scaling. The new method applies exponential transformation, which converts the Hankel transforms (eqs 30 and 31) into cross-correlations (eqs 37 and 38). Therefore, the efficient implementation of the FFT algorithm can be directly applied for calculating those computationally expensive convolutions (eqs 6, 10, 15, and 16) in density functional theory. The scaling of the new algorithm is not the best because of the nonequidistant grids. However, it shows an excellent speedup for the system of a small domain size in Figure 3. This makes the algorithm especially efficient for the study of fluid adsorption in a nanopore of zeolites, which have a pore size of a few angstroms. Transform methods also provide additional speedup because the weighting functions in fundamental measure theory have closed-form solutions in Fourier space, and they can be evaluated in $O(1)$ operation, as seen in the Supporting Information. This further explains why the transform methods are always faster than the elliptic function method. For the calculations of methane adsorption, the improvement is less significant than hard-sphere fluids but faster by one order of magnitude. The free energy density

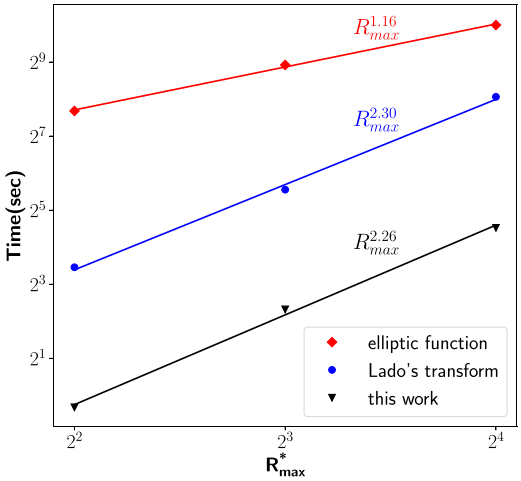

Figure 3. Time scaling for hard-spheres at reduced bulk density $\rho^*_{\text{B}} = 0.8$ adsorbed in hard cylindrical pores of varying pore sizes. The convergence time for each algorithm is measured on a single desktop machine of Intel Core i7-6700 processor with a base frequency 3.40 GHz.

https://dx.doi.org/10.1021/acs.iecr.9b06895
Ind. Eng. Chem. Res. 2020, 59, 6716−6728

derivative with respect to weighted densities in eq 10 requires many local calculations at each grid point. This is because of the universal integrals I_1 and I_2 in eq 9 from the second-order perturbation contributions in PC-SAFT.[32] These calculations scale as $O(cN)$ with N as the number of mesh grid and c represents the number of computational operations of the PC-SAFT dispersion term during implementation. As N can also be a large number for nonequidistant mesh grids, this step undermines the overall performances for systems with this kind of dispersion term.

The Hankel transform can be regarded as an expansion of a function by Fourier−Bessel series. The Gibbs phenomenon is observed where the function has a jump discontinuity.[39] It is interesting that the Fourier−Bessel expansion exhibits a Gibbs-like phenomenon close to the origin. Gray and Pinsky[40] showed that the asymptotic behavior of Fourier−Bessel series has a slower rate of convergence at the origin than at surrounding points. For the zeroth-order Fourier−Bessel expansion, which is the basis for the Hankel transform in this work, of $f(r) = 1$ and its asymptotic behavior when $k \to \infty$ and $r \neq 0$ is[40]

$$\frac{(-1)^{k-1}\cos((1 + r - 4kr)\pi/4)}{(k - 1/4)\pi\sqrt{r}} + O\left(\frac{1}{k^2}\right) \tag{45}$$

For $k \to \infty$ and $r = 0$, the asymptotic form of $f(r) = 1$ is

$$\frac{(-1)^{k-1}\sqrt{2}}{\sqrt{4k - 1}} + O\left(\frac{1}{k^{3/2}}\right) \tag{46}$$

The rate of convergence at the origin is $O\left(\frac{1}{k^{3/2}}\right)$ and its surrounding converges at a faster rate of $O\left(\frac{1}{k^2}\right)$. The Gibbs-like phenomenon at the origin can cause a divergence at the origin of a cylindrical pore in density functional theory. Adding the correction factor to the origin in eq 42 can improve the stability of the solution method. A situation is demonstrated in Figure 4 where a system solved by a maximum grid spacing of $\Delta r^* = 3 \times 10^{-3}$ without including the error correction term at the origin diverges.

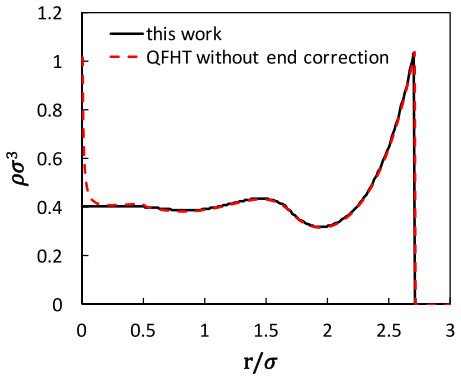

Figure 4. Solution provided by our method (solid line) and solution provide by QFHT (dashed line) for hard-sphere fluid in a hard cylindrical pore with $R^* = 3$ and bulk density $\rho_B^* = 0.4$ with a maximum mesh size $\Delta r^* = 3 \times 10^{-3}$. QFHT does not include a correction factor at the origin.

5. APPLICATION OF THE ALGORITHM FOR ISAFT

5.1. Methane Adsorbed under a Cylindrical Steele 10-4-3 Attractive Potential. The phase behavior of hydrocarbons in nanoscale pores is important for oil and natural gas production from tight formations[41] and chemical processing.[42] The study of phase behavior of hydrocarbons under reservoir conditions requires an inhomogeneous thermodynamic model for hydrocarbons and surface potential. Previously, DFT has been applied to model alkane adsorption in mesoporous silica using smooth wall approximation for MCM-41[43] and SBA-15.[44] Recently, the surface roughness and random surface effect have also been studied using SAFT-based DFT by Aslyamov et al.[45] In this section, we show that iSAFT with the recently developed cylindrical Steele 10-4-3 potential can be used to study the fluid distribution of methane molecules in graphite cylindrical nanopores by applying the new numerical algorithm. The modeling of methane adsorption requires several parameters to characterize the physical properties of methane, graphite wall, and the interaction between methane and graphite.

The external potential used here is the Steele 10-4-3[46] type of cylindrical potential provided by Siderius and Gelb.[47] The cylindrical Lennard-Jones (LJ) 9-3 potential[48,49] and the potential by Tjatjopoulos et al.[50] have been exploited in previous studies of fluid adsorption in cylindrical pores. The potential by Tjatjopoulos has been successfully applied to model adsorption in MCM-41 type materials and single-wall carbon nanotubes. It suffers from the fact that this potential is based on a single cylindrical shell model. Therefore, it does not describe a confining wall with a multilayer structure, and it cannot reduce to the Steele 10-4-3 potential in the infinite large pore limit. The cylindrical Steele 10-4-3 potential is dependent on the radial distance to the surface and pore radius. It is given as[47]

$$V^{10-4-3}(r, R) = 2\pi\rho_s\Delta\sigma_s^2\epsilon_s\left[\psi_6(r, R, \sigma_s) - \psi_3(r, R, \sigma_s) - \frac{\sigma_s}{\Delta}\phi_3(r, R + \alpha\Delta, \sigma_s)\right] \tag{47}$$

where ρ_s, ϵ_s, Δ, and σ_s are parameters of the solid wall to represent the interactions between solid atoms and fluid molecules.

The term $\phi_n(r, R, \sigma_s)$ can be calculated

$$\phi_n(r, R, \sigma_s) = \frac{4\sqrt{\pi}\Gamma\left(n-\frac{1}{2}\right)}{(2n - 3)\Gamma(n)}\left(\frac{\sigma_s}{R}\right)^{2n-3}\left[1 - \left(\frac{r}{R}\right)^2\right]^{3-2n} F\left[\frac{3 - 2n}{2}, \frac{5 - 2n}{2}; 1; \left(\frac{r}{R}\right)^2\right]$$

and $\psi_n(r, R, \sigma_s)$ can be calculated

$$\psi_n(r, R, \sigma_s) = \frac{4\sqrt{\pi}\Gamma\left(n-\frac{1}{2}\right)}{\Gamma(n)}\left(\frac{\sigma_s}{R}\right)^{2n-2}\left[1 - \left(\frac{r}{R}\right)^2\right]^{2-2n} F\left[\frac{3 - 2n}{2}, \frac{3 - 2n}{2}; 1; \left(\frac{r}{R}\right)^2\right]$$

where $F(a, b; c; z)$ denotes the Gaussian hypergeometric function, $\Gamma(n)$ is the gamma function, and R is the radius of the cylindrical pore. It can be shown that this cylindrical Steele potential reduces to the planar Steele potential in the limit of

https://dx.doi.org/10.1021/acs.iecr.9b06895
Ind. Eng. Chem. Res. 2020, 59, 6716−6728

infinitely large pore.[47] The pure-component parameters for methane used in this study from PC-SAFT[32] are m = 1, σ = 3.7039 Å, and ϵ/k_B = 150.03 K. The binary interaction parameters are provided in Table 1. The interaction parameters between methane and graphite are obtained using the Berthelot−Lorentz combining rules. α in eq 47 is set as 0.61 as empirical treatment.

Table 1. DFT Parameters for Methane Adsorption in Graphite Carbon Nanopore

component	σ (nm)	ϵ/k_B (K)	ρ_s (nm^{-3})	Δ (nm)
CH_4	0.37039	150.03	N.A.	N.A.
graphite	0.34000	28.00	114	0.335
CH_4−graphite	0.35520	64.81	N.A.	N.A.

In Figure 5a, we present the microscopic density profile for methane adsorbed in a large cylindrical pore at R = 18.55 Å at 150 K. Two microscopic pictures of methane correspond to the profile before and after capillary condensation. Microscopic fluid structures of methane adsorbed in a small pore of R = 11.13 Å at 105 K are shown in Figure 5b. The exceptionally high microscopic density at the center of the pore, that is due to packing effect, is well demonstrated in Figure 5b.

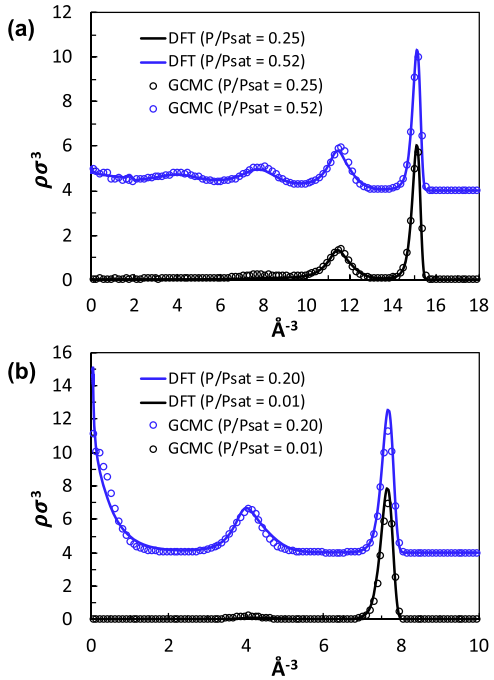

Figure 5. Density profiles of methane adsorbed in cylindrical nanopores of radius R = 18.55 Å at 150 K (a) and R = 11.13 Å at T = 105 K (b). Methane bulk pressures are set as 0.52 and 0.25 P_{sat} in (a), 0.20, and 0.01 P_{sat} in (b). Solid lines represent density functional theory results using the new algorithm. Markers represent our molecular simulation results.

Figures 6 and 7 show the adsorption isotherm of methane for a cylindrical pore of radius R = 11.13 and 18.55 Å. The adsorption is defined by

$$\Gamma = 2/R^2 \int_0^R \rho(r) r \, dr \tag{48}$$

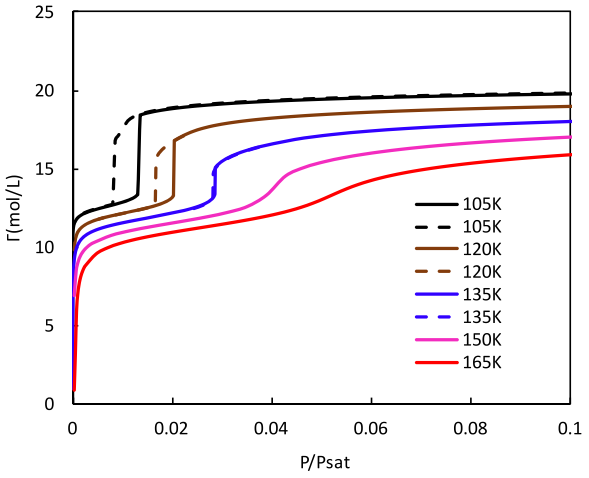

Figure 6. Methane adsorption isotherm in a cylindrical nanopore of radius R = 11.13 Å. Isotherms are calculated by DFT at temperatures T = 105, 120, 135, 150, and 165 K. Dashed lines and solid lines refer to desorption and adsorption, respectively.

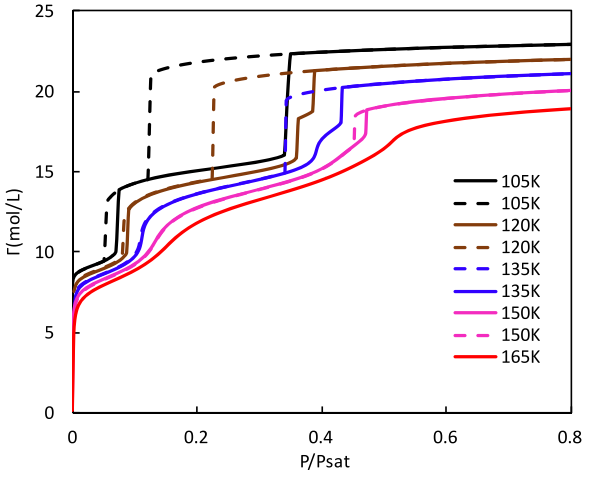

Figure 7. Methane adsorption isotherm in a cylindrical nanopore of radius R = 18.55 Å. Isotherms are calculated by DFT at temperatures T = 105, 120, 135, 150, and 165 K. Dashed lines and solid lines refer to desorption and adsorption, respectively.

where R is the radius of a cylindrical pore. For a smaller nanopore of radii R = 11.13 Å, a single hysteresis loop is found at T = 105, 120, and 135 K, which indicates first-order capillary condensations. Sharp layering transitions are also found for methanes adsorbed in a large nanopore of pore radii R = 18.55 Å at 105 and 120 K. Ball and Evans[51] applied the mean-field smoothed density approximation (SDA) density functional theory to study the layering transition of Yukawa fluids under a single wall and cylindrical walls of van der Waals potential. They concluded that the layering transition predicted by density functional theory occur at a temperature below the triple point. A similar argument is made by Peterson et al.[48] in a study of LJ fluids' adsorption in cylindrical pores of smeared-out LJ 9-3 potentials using mean-field density functional theory. They found that discontinuous first-order layering transitions only occurred below bulk triple point, and the sharp layering transition degraded into a smoothed transition at or above the triple point. Discontinuous layering transition at temperatures above triple points, however, have been reported from well-designed experimental studies of methane adsorp-

https://dx.doi.org/10.1021/acs.iecr.9b06895
Ind. Eng. Chem. Res. 2020, 59, 6716−6728

tion[52] and ethylene adsorption on graphite.[53] In our study, sharp first-order layering transitions are found in Figure 7 given that the triple point for methane is 90.67 K. We attribute the predicted layering transition above triple point in this study to the non-mean-field dispersion free energy functional and the application of cylindrical Steele potential.

The bulk critical point of methane is 190.6 K. Figures 6 and 7 show that the critical points for methane under a cylindrical nanopore of R = 11.13 and 18.55 Å are much lower than methane's bulk critical point. We made no attempt to locate the exact critical points for methanes adsorbed in graphite cylindrical pores. However, the impact of nanopore curvature on critical points is immediate from a comparison to adsorption in slit-pore. Liu et al. studied the critical points of methane adsorption in slit-like pores under Steele potential by iSAFT and compared the predicted critical points with GCMC simulation.[19] For methane in slit-like pore of width 2 nm, the critical point predicted by iSAFT is 158 K. In Figure 6, methane adsorbed in a cylindrical pore of diameter 2.2 nm at 150 K is in a supercritical state. The lowered critical point for methane adsorption in the cylindrical pore is due to stronger eccentric confinement.

5.2. Modeling Bottlebrush Polymers. Polymer brushes are a class of well-designed polymers that are grafted by one end to surfaces of various shapes. Bottlebrush polymer refers to 1D polymer brushes grafted to a cylindrical backbone.[54] The well-studied synthesis for bottlebrush polymer and its enriched architecture lead to many applications. For example, Djalali et al. used nanogold as a backbone for bottlebrush polymers and the hybrid metallic and cylindrical polymer brushes can be used as nanowires.[55] Zhang et al. grafted amphiphilic polymer brushes to a backbone of carboxylate groups. Because of the affinity of carboxylate groups to metal ions, this bottlebrush polymer can be used as a cylindrical molecular nanoreactor.[56,57]

Modeling bottlebrush polymers is a challenging task because of the length-scale of the system. Self-consistent field theory (SCFT) is a popular theoretical tool for modeling bottlebrush polymers. Unlike density functional theory, none of the variations of SCFT[58,59] can capture local packing effect and layering effect, which are important for understanding solvent distributions and solvation forces.[29] DFT has been used to model the structure of planar polymer brushes[60−62] and spherical polymer brushes.[63] Significant numerical efforts are required for modeling bottlebrush polymers by DFT because of cylindrical geometry.[29] Here, we use iSAFT to model bottlebrush polymers in implicit solvent. Segments interact with each other by hard-sphere repulsion and tangential bonding. Further details of the molecular model for grafted polymers can be found in our previous study of polymer brushes tethered to flat surfaces.[64] The details of molecular dynamics simulation that we compare theoretical results with are given in the Supporting Information.

The iSAFT free energy functional of bottlebrush polymers in this study has ideal contribution, hard-sphere contribution, and chain contribution, which are given in Section 2. The contribution of solvents and dispersion will be subjects of future work. To tether the polymers onto a cylindrical backbone, we need to add an external potential. The end segment that is grafted to a backbone is under an external potential

$$V_1^{\text{ext}}(r) = \begin{cases} v & \text{if} \quad r = (R + \sigma_\alpha/2) \\ \infty & \text{otherwise} \end{cases} \tag{49}$$

and for the other segments

$$V_\alpha^{\text{ext}}(r) = \begin{cases} \infty & \text{for} \quad r \le (R + \sigma_\alpha/2) \\ 0 & \text{otherwise} \end{cases} \tag{50}$$

where R is the backbone radius of bottlebrush polymers and σ_α is the segment diameter of polymers. The segment diameter is not temperature-dependent since the system is athermal.

The density profile for end segment can be calculated from eq 17

$$\rho_1(0) = \exp(\beta\mu_M) \exp[D_1(0) - \beta v] I_{1,1}(0) I_{2,1}(0)$$

and for the other segments

$$\rho_\alpha(r_\alpha) = \exp(\beta\mu_M) \exp[D_1(0) - \beta v] \exp[D_\alpha(r_\alpha)] I_{1,\alpha}(r_\alpha) I_{2,\alpha}(r_\alpha), \quad \text{for } r_\alpha > R + \frac{\sigma_\alpha}{2} \tag{51}$$

Chain connectivity for all of the segments of bottlebrush polymers are modeled by the recursive integrals $I_{1,\alpha}$ and $I_{2,\alpha}$ in Section 2 except that

$$I_{1,1}(r_1) = 1$$

$$I_{1,2}(r_2) = \Delta^{1,2}(0, r_2), \quad \text{for} \quad r_2 > R + \frac{\sigma_2}{2}$$

$$I_{1,\alpha}(r_\alpha) = \int I_{1,\alpha-1}(r_{\alpha-1}) \exp[D_{\alpha-1}(r_{\alpha-1})] \Delta^{\alpha-1,\alpha}(r_{\alpha-1}, r_\alpha) \, dr_{\alpha-1}, \quad \text{for} \quad r_\alpha > R + \frac{\sigma_\alpha}{2}$$

and

$$I_{2,m}(r_\alpha) = 1$$

$$I_{2,\alpha}(r_\alpha) = \int I_{2,\alpha+1}(r_{\alpha+1}) \exp[D_{\alpha+1}(r_{\alpha+1})] \Delta^{\alpha,\alpha+1}(r_\alpha, r_{\alpha+1}) \, dr_{\alpha+1}, \quad \text{for} \quad r_\alpha > R + \frac{\sigma_\alpha}{2}$$

$$I_{2,1}(0) = \int I_{2,2}(r_2) \exp[D_2(r_2)] \Delta^{1,2}(0, r_2) \, dr_2, \quad \text{for } r_2 > R + \frac{\sigma_2}{2}$$

The external potential v for the first segment in eqs 49 and 51 is calculated from the grafting density ρ_g of bottlebrush polymers

$$\rho_g = \int dr_1 \, \rho_1(r_1) r_1 = \exp[\beta\mu_M] \exp[D_1(0) - \beta v] I_{1,1}(0) I_{2,1}(0) \tag{52}$$

then, density profiles for all segments are

$$\rho_\alpha(r_\alpha) = \frac{\rho_g}{I_{1,1}(0) I_{2,1}(0)} \exp[D_\alpha(r_\alpha)] I_{1,\alpha}(r_\alpha) I_{2,\alpha}(r_\alpha), \quad \text{for } r_\alpha > R + \frac{\sigma_\alpha}{2} \tag{53}$$

Figure 8 shows the distribution of polymer brushes grafted to a planar surface (a) and to a cylindrical surface for bottlebrush polymers (b). The backbone radius R is set to 1σ. A small radii means a large curvature, which can effectively

https://dx.doi.org/10.1021/acs.iecr.9b06895
Ind. Eng. Chem. Res. 2020, 59, 6716−6728

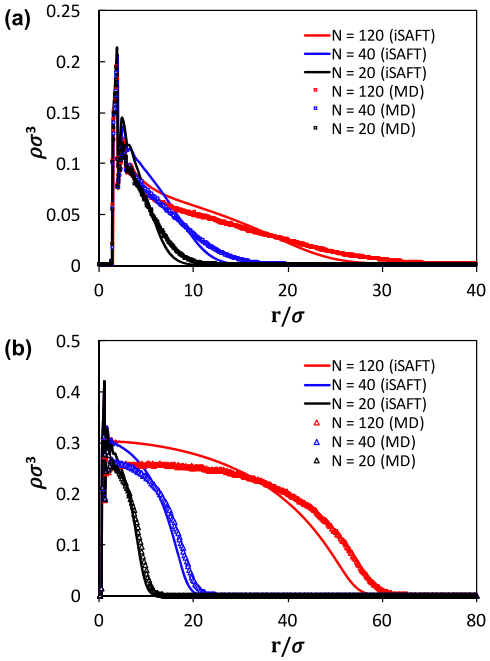

Figure 8. Segment density profiles of hard-sphere chains of varying lengths tethered to surface of different geometries. (a) Polymer brushes tethered to cylindrical surface. (b) Polymer brushes tethered to flat surface. Solid lines are iSAFT predictions. (□) represent MD simulation results for cylindrical surfaces. (△) represent MD simulation results for flat surfaces. Chain length N varies from 20 to 120.

differentiate the bottlebrush polymers in Figure 8a from planar polymer brushes in Figure 8b. The grafting densities of (a) and (b) are fixed at $\rho_g\sigma^3 = 0.1$. The chain lengths of polymer brushes range from 20 to 120. A power-law shape is observed for a bottlebrush polymer profile and a parabolic shape is observed for polymer grafted to a flat surface. This also agrees with the study by Wijmans and Zhulina[65] using the analytical self-consistent field (SCF) model. The curvature effects from the surface shape lead to different levels of repulsive force exerted onto monomers. The spans of polymer brush density distributions, as seen in Figure 8a,b, imply different scaling laws for the radius of gyration, which is confirmed by other studies.[65,66]

Figure 9 shows how the microstructure of polymer brushes vary for different curvatures at fixed grafting density and fixed chain length. As the radius of bottlebrush backbone increases, a continual transition from a power-law to parabolic distribution is observed. A flat surface can be treated as a limiting case of infinitely large radius. The density of the adsorbed polymers close to backbones also increases because larger radii result in stronger entropic repulsive forces. It can be seen that the convergence process toward a zero curvature flat wall is very slow. This is also found by Roth et al. in a study of depletion force exerted by curved surfaces.[24]

6. CONCLUSIONS

iSAFT has been successful in modeling the behaviors of inhomogeneous fluids. A numerical challenge however existed for the application of iSAFT to fluids in cylindrical geometry. We have presented an efficient numerical solution method in resolving this problem by using fast Hankel transform on a nonequidistant grid. Improvement in numerical efficiency and time scaling are achieved. Two applications of the methods are discussed. Interesting physical insights are obtained including theory predicts layering transitions above the triple point for methane adsorption in nanopores and theory captures power-law to parabolic transitions of polymer brush microstructure. We conclude that the continuous development of solution algorithm for iSAFT enables researchers to investigate curvature effects for fluids in an efficient manner.

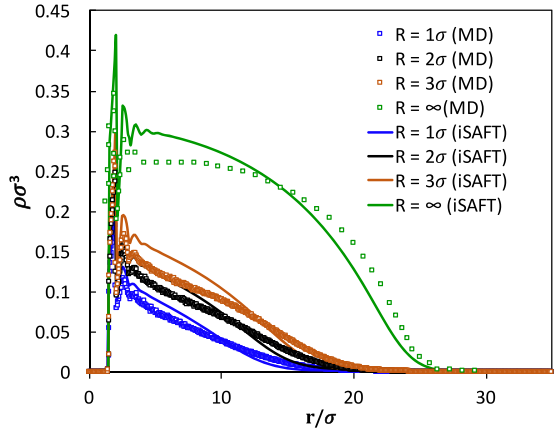

Figure 9. Segment density profiles of bottlebrush polymers and planar polymer brushes. R stands for the backbone radius of bottlebrush polymers. Bottlebrush polymers are in blue, black, and brown. Planar polymer brushes are in green. Solid lines represent iSAFT results. □ represent molecular dynamics simulation results. Details of MD simulation for bottlebrush polymers are provided in the Supporting Information. MD simulation of planar polymer brushes are from the study by Grest et al.[67]

■ ASSOCIATED CONTENT

Supporting Information

The Supporting Information is available free of charge at https://pubs.acs.org/doi/10.1021/acs.iecr.9b06895.

Molecular simulation details; free energy functional derivatives for hard-sphere contribution in cylindrical geometry; Fourier transform of weighting functions (PDF)

■ AUTHOR INFORMATION

Corresponding Author

Walter G. Chapman − *Department of Chemical and Biomolecular Engineering, Rice University, Houston, Texas 77005, United States;* orcid.org/0000-0002-8789-9041; Email: wgchap@rice.edu

Authors

Shun Xi − *Department of Chemical and Biomolecular Engineering, Rice University, Houston, Texas 77005, United States;* orcid.org/0000-0001-5651-6207

Jinlu Liu − *Department of Chemical and Biomolecular Engineering, Rice University, Houston, Texas 77005, United States;* orcid.org/0000-0002-7781-7153

Arjun Valiya Parambathu − *Department of Chemical and Biomolecular Engineering, Rice University, Houston, Texas 77005, United States;* orcid.org/0000-0003-2620-9534

Yuchong Zhang − *Department of Chemical and Biomolecular Engineering, Rice University, Houston, Texas 77005, United States;* orcid.org/0000-0002-6809-1020

https://dx.doi.org/10.1021/acs.iecr.9b06895
Ind. Eng. Chem. Res. 2020, 59, 6716−6728

Complete contact information is available at:
https://pubs.acs.org/10.1021/acs.iecr.9b06895

Notes

The authors declare no competing financial interest.

■ ACKNOWLEDGMENTS

The authors thank Philipp Rehner for constructive feedback to the manuscript. The authors also thank Dr. Chen Liu for insightful discussions. The research was supported by the Robert A. Welch Foundation (Grant No. C-1241).

■ REFERENCES

(1) Rosenfeld, Y. Free-energy model for the inhomogeneous hard-sphere fluid mixture and density-functional theory of freezing. *Phys. Rev. Lett.* **1989**, *63*, 980.
(2) Wu, J. Density functional theory for chemical engineering: From capillarity to soft materials. *AIChE J.* **2006**, *52*, 1169−1193.
(3) Emborsky, C. P.; Feng, Z.; Cox, K. R.; Chapman, W. G. Recent advances in classical density functional theory for associating and polyatomic molecules. *Fluid Phase Equilib.* **2011**, *306*, 15−30.
(4) Roth, R. Fundamental measure theory for hard-sphere mixtures: a review. *J. Phys.: Condens. Matter* **2010**, *22*, No. 063102.
(5) Wang, L.; Haghmoradi, A.; Liu, J.; Xi, S.; Hirasaki, G. J.; Miller, C. A.; Chapman, W. G. Modeling micelle formation and interfacial properties with iSAFT classical density functional theory. *J. Chem. Phys.* **2017**, *146*, No. 124705.
(6) Malijevskỳ, A. Fundamental measure theory in cylindrical geometry. *J. Chem. Phys.* **2007**, *126*, No. 134710.
(7) Sears, M. P.; Frink, L. J. A new efficient method for density functional theory calculations of inhomogeneous fluids. *J. Comput. Phys.* **2003**, *190*, 184−200.
(8) Grella, R. Fresnel propagation and diffraction and paraxial wave equation. *J. Opt.* **1982**, *13*, 367.
(9) Gottlieb, D.; Orszag, S. A. *Numerical Analysis of Spectral Methods: Theory and Applications*; CBMS-NSF Regional Conference Series in Applied Mathematics; Society for Industrial and Applied Mathematics, 1977; Vol. *26*.
(10) Bisseling, R.; Kosloff, R. The fast Hankel transform as a tool in the solution of the time dependent Schrödinger equation. *J. Comput. Phys.* **1985**, *59*, 136−151.
(11) Lado, F. Numerical Fourier transforms in one, two, and three dimensions for liquid state calculations. *J. Comput. Phys.* **1971**, *8*, 417−433.
(12) Siegman, A. Quasi fast Hankel transform. *Opt. Lett.* **1977**, *1*, 13−15.
(13) Gardner, D. G.; Gardner, J. C.; Laush, G.; Meinke, W. W. Method for the analysis of multicomponent exponential decay curves. *J. Chem. Phys.* **1959**, *31*, 978−986.
(14) Magni, V.; Cerullo, G.; De Silvestri, S. High-accuracy fast Hankel transform for optical beam propagation. *J. Opt. Soc. Am. A* **1992**, *9*, 2031−2033.
(15) Tripathi, S.; Chapman, W. G. Microstructure of inhomogeneous polyatomic mixtures from a density functional formalism for atomic mixtures. *J. Chem. Phys.* **2005**, *122*, No. 094506.
(16) Jain, S.; Dominik, A.; Chapman, W. G. Modified interfacial statistical associating fluid theory: A perturbation density functional theory for inhomogeneous complex fluids. *J. Chem. Phys.* **2007**, *127*, No. 244904.
(17) Chapman, W. G.; Gubbins, K. E.; Jackson, G.; Radosz, M. SAFT: Equation-of-state solution model for associating fluids. *Fluid Phase Equilib.* **1989**, *52*, 31−38.
(18) Ballal, D.; Chapman, W. G. Hydrophobic and hydrophilic interactions in aqueous mixtures of alcohols at a hydrophobic surface. *J. Chem. Phys.* **2013**, *139*, No. 114706.
(19) Liu, J.; Wang, L.; Xi, S.; Asthagiri, D.; Chapman, W. G. Adsorption and Phase Behavior of Pure/Mixed Alkanes in Nanoslit Graphite Pores: An iSAFT Application. *Langmuir* **2017**, *33*, 11189−11202.
(20) Emborsky, C. P.; Cox, K. R.; Chapman, W. G. Exploring parameter space effects on structure-property relationships of surfactants at liquid-liquid interfaces. *J. Chem. Phys.* **2011**, *135*, No. 084708.
(21) Zhang, Y.; Valiya Parambathu, A.; Chapman, W. G. Density functional study of dendrimer molecules in solvents of varying quality. *J. Chem. Phys.* **2018**, *149*, No. 064904.
(22) Bymaster, A.; Chapman, W. G. An i SAFT density functional theory for associating polyatomic molecules. *J. Phys. Chem. B* **2010**, *114*, 12298−12307.
(23) Fisher, L.; Gamble, R.; Middlehurst, J. The Kelvin equation and the capillary condensation of water. *Nature* **1981**, *290*, 575−576.
(24) Roth, R.; Götzelmann, B.; Dietrich, S. Depletion forces near curved surfaces. *Phys. Rev. Lett.* **1999**, *83*, 448.
(25) Bryk, P.; Roth, R.; Mecke, K.; Dietrich, S. Hard-sphere fluids in contact with curved substrates. *Phys. Rev. E* **2003**, *68*, No. 031602.
(26) Forsman, J.; Woodward, C. E. Colloidal interactions in thermal and athermal polymer solutions: The Derjaguin approximation, and exact results for mono-and polydisperse ideal chains. *J. Chem. Phys.* **2009**, *131*, No. 044903.
(27) Derjaguin, B. V. Untersuchungen über die Reibung und Adhäsion, IV. *Kolloid-Z.* **1934**, *69*, 155−164.
(28) Hlushak, S. Heat of adsorption, adsorption stress, and optimal storage of methane in slit and cylindrical carbon pores predicted by classical density functional theory. *Phys. Chem. Chem. Phys.* **2018**, *20*, 872−888.
(29) Binder, K.; Egorov, S.; Milchev, A. Polymer Brushes on Flat and Curved Substrates: What Can be Learned from Molecular Dynamics Simulations. In *Polymer and Biopolymer Brushes: for Materials Science and Biotechnology*; John Wiley & Sons, Inc., 2017; Vols. *I and II*, pp 141−159.
(30) Bymaster, A.; Jain, S.; Chapman, W. G. Microstructure and depletion forces in polymer-colloid mixtures from an interfacial statistical associating fluid theory. *J. Chem. Phys.* **2008**, *128*, No. 164910.
(31) Xi, S.; Wang, L.; Liu, J.; Chapman, W. Thermodynamics, Microstructures, and Solubilization of Block Copolymer Micelles by Density Functional Theory. *Langmuir* **2019**, *35*, 5081−5092.
(32) Gross, J.; Sadowski, G. Perturbed-chain SAFT: An equation of state based on a perturbation theory for chain molecules. *Ind. Eng. Chem. Res.* **2001**, *40*, 1244−1260.
(33) Sauer, E.; Gross, J. Classical density functional theory for liquid−fluid interfaces and confined systems: A functional for the perturbed-chain polar statistical associating fluid theory equation of state. *Ind. Eng. Chem. Res.* **2017**, *56*, 4119−4135.
(34) Segura, C. J.; Chapman, W. G. Associating fluids with four bonding sites against solid surfaces: Monte Carlo simulations. *Mol. Phys.* **1995**, *86*, 415−442.
(35) Segura, C. J.; Vakarin, E. V.; Chapman, W. G.; Holovko, M. A comparison of density functional and integral equation theories vs Monte Carlo simulations for hard sphere associating fluids near a hard wall. *J. Chem. Phys.* **1998**, *108*, 4837−4848.
(36) Agrawal, G. P.; Lax, M. End correction in the quasi-fast Hankel transform for optical-propagation problems. *Opt. Lett.* **1981**, *6*, 171−173.
(37) Boţan, V.; Pesth, F.; Schilling, T.; Oettel, M. Hard-sphere fluids in annular wedges: Density distributions and depletion potentials. *Phys. Rev. E* **2009**, *79*, No. 061402.
(38) Harrison, J. In *Fast and Accurate Bessel Function Computation*, 2009 19th IEEE Symposium on Computer Arithmetic, 2009; pp 104−113.
(39) Gottlieb, D.; Shu, C.-W. On the Gibbs phenomenon and its resolution. *SIAM Rev.* **1997**, *39*, 644−668.
(40) Gray, A.; Pinsky, M. A. Computer Graphics and a New Gibbs Phenomenon for Fourier−Bessel Series. *Exp. Math.* **1992**, *1*, 313−316.

(41) Ratner, M.; Tiemann, M. *An Overview of Unconventional Oil and Natural Gas: Resources and Federal Actions*, CRS Report; Congressional Research Service, 2014.
(42) Fechete, I.; Vedrine, J. C. Nanoporous materials as new engineered catalysts for the synthesis of green fuels. *Molecules* **2015**, *20*, 5638−5666.
(43) Cao, D.; Shen, Z.; Chen, J.; Zhang, X. Experiment, molecular simulation and density functional theory for investigation of fluid confined in MCM-41. *Microporous Mesoporous Mater.* **2004**, *67*, 159−166.
(44) Ravikovitch, P. I.; Neimark, A. V. Characterization of micro-and mesoporosity in SBA-15 materials from adsorption data by the NLDFT method. *J. Phys. Chem. B* **2001**, *105*, 6817−6823.
(45) Aslyamov, T.; Pletneva, V.; Khlyupin, A. Random surface statistical associating fluid theory: Adsorption of n-alkanes on rough surface. *J. Chem. Phys.* **2019**, *150*, No. 054703.
(46) Steele, W. A. The physical interaction of gases with crystalline solids: I. Gas-solid energies and properties of isolated adsorbed atoms. *Surf. Sci.* **1973**, *36*, 317−352.
(47) Siderius, D. W.; Gelb, L. D. Extension of the Steele 10-4-3 potential for adsorption calculations in cylindrical, spherical, and other pore geometries. *J. Chem. Phys.* **2011**, *135*, No. 084703.
(48) Peterson, B. K.; Walton, J. P.; Gubbins, K. E. Fluid behaviour in narrow pores. *J. Chem. Soc., Faraday Trans. 2* **1986**, *82*, 1789−1800.
(49) Zhang, X.; Wang, W.; Jiang, G. A potential model for interaction between the Lennard-Jones cylindrical wall and fluid molecules. *Fluid Phase Equilib.* **2004**, *218*, 239−246.
(50) Tjatjopoulos, G. J.; Feke, D. L.; Mann, J. A., Jr. Molecule-micropore interaction potentials. *J. Phys. Chem. A* **1988**, *92*, 4006−4007.
(51) Ball, P.; Evans, R. Structure and adsorption at gas-solid interfaces: Layering transitions from a continuum theory. *J. Chem. Phys.* **1988**, *89*, 4412−4423.
(52) Inaba, A.; Koga, Y.; Morrison, J. A. Multilayers of methane adsorbed on graphite. *J. Chem. Soc., Faraday Trans. 2* **1986**, *82*, 1635−1646.
(53) Drir, M.; Nham, H.; Hess, G. B. Multilayer adsorption and wetting: Ethylene on graphite. *Phys. Rev. B: Condens. Matter Mater. Phys.* **1986**, *33*, 5145.
(54) Zhang, M.; Müller, A. H. Cylindrical polymer brushes. *J. Polym. Sci., Part A: Polym. Chem.* **2005**, *43*, 3461−3481.
(55) Djalali, R.; Li, S.-Y.; Schmidt, M. Amphipolar core- shell cylindrical brushes as templates for the formation of gold clusters and nanowires. *Macromolecules* **2002**, *35*, 4282−4288.
(56) Zhang, M.; Estournes, C.; Bietsch, W.; Müller, A. Superparamagnetic hybrid nanocylinders. *Adv. Funct. Mater.* **2004**, *14*, 871−882.
(57) Zhang, M.; Drechsler, M.; Müller, A. H. Template-controlled synthesis of wire-like cadmium sulfide nanoparticle assemblies within core- shell cylindrical polymer brushes. *Chem. Mater.* **2004**, *16*, 537−543.
(58) Szleifer, I.; Carignano, M. Tethered polymer layers. *Adv. Chem. Phys.* **1996**, *94*, 165−260.
(59) Scheutjens, J.; Fleer, G. Statistical theory of the adsorption of interacting chain molecules. 1. Partition function, segment density distribution, and adsorption isotherms. *J. Phys. Chem. B* **1979**, *83*, 1619−1635.
(60) Gong, K.; Chapman, W. G. Solvent response of mixed polymer brushes. *J. Chem. Phys.* **2011**, *135*, No. 214901.
(61) Gong, K.; Marshall, B. D.; Chapman, W. G. Response behavior of diblock copolymer brushes in explicit solvent. *J. Chem. Phys.* **2012**, *137*, No. 154904.
(62) Gong, K.; Marshall, B. D.; Chapman, W. G. Modeling lower critical solution temperature behavior of associating polymer brushes with classical density functional theory. *J. Chem. Phys.* **2013**, *139*, No. 094904.
(63) Lo Verso, F.; Egorov, S. A.; Milchev, A.; Binder, K. Spherical polymer brushes under good solvent conditions: Molecular dynamics results compared to density functional theory. *J. Chem. Phys.* **2010**, *133*, No. 184901.
(64) Jain, S.; Jog, P.; Weinhold, J.; Srivastava, R.; Chapman, W. G. Modified interfacial statistical associating fluid theory: Application to tethered polymer chains. *J. Chem. Phys.* **2008**, *128*, No. 154910.
(65) Wijmans, C.; Zhulina, E. B. Polymer brushes at curved surfaces. *Macromolecules* **1993**, *26*, 7214−7224.
(66) Milner, S. T.; Witten, T.; Cates, M. Theory of the grafted polymer brush. *Macromolecules* **1988**, *21*, 2610−2619.
(67) Grest, G. S.; Murat, M. Structure of grafted polymeric brushes in solvents of varying quality: a molecular dynamics study. *Macromolecules* **1993**, *26*, 3108−3117.

https://dx.doi.org/10.1021/acs.iecr.9b06895
Ind. Eng. Chem. Res. 2020, 59, 6716−6728